Vorticity Elongation in Polymeric Emulsions

E. K. Hobbie and K. B. Migler

National Institute of Standards and Technology,
Gaithersburg, Maryland 20899
(Received 16 October 1998)

Video microscopy is used to measure the shear-induced deformation of dilute emulsions composed of viscoelastic polymer melts. In the limit of strong shear, a transition in which the droplets elongate perpendicular to the flow field is observed. A force-balance argument relates this behavior to the change in first normal stress difference across the droplet interface.   [S0031-9007(99)09504-6]

When a fluid dispersed in a second fluid is subjected to shear, the droplets deform and burst, and the use of shear flow to emulsify immiscible liquids is ubiquitous in the processing of soft materials. Although the pioneering work of Taylor [1–4] on isolated Newtonian emulsions remains at the foundation of our understanding, with the underlying intuition that the droplets elongate along the direction of flow at sufficiently high shear rates, the shear response of fluids that exhibit rheological complexity, such as semidilute entangled polymer solutions [5–8], wormlike micelles [9], and thixotropic clay gels [10], suggests that the shear can induce domains with extended correlation along the direction of *vorticity,* perpendicular to the flow field. In this Letter, stroboscopic video microscopy is used to measure the shear response of dilute emulsions composed of viscoelastic polymer melts. At low shear rates, the behavior is in agreement with the Taylor picture. In the limit of strong shear, however, the droplets become extended along the vorticity axis, and a simple force-balance argument is presented that relates this unusual transition to the change in first normal stress difference across the droplet interface.

The pressure-driven optical flow cell [11] is shown schematically in Fig. 1. The instrument easily achieves shear rates at which elastic stresses in the melt become much larger than the shear stress, which typically cannot be achieved in a rotating-geometry device. The shear rate ($\dot{\gamma}$) is a function of the distance from one of the walls, and the measurements presented here were taken at the surface of the bottom window [12]. The materials are polystyrene (PS) and polyethylene (PE) at $T = 195\,°C$, with molecular weights [13] $M_w = 195 \times 10^3$ ($M_n = 83 \times 10^3$) for PS_1, $M_w = 342 \times 10^3$ ($M_n = 141 \times 10^3$) for PS_2, $M_w = 85.2 \times 10^3$ ($M_n = 15.4 \times 10^3$) for PE_1, and $M_w = 83.1 \times 10^3$ ($M_n = 25.6 \times 10^3$) for PE_2, where PE_1 is low-density with long-chain branching and PE_2 is linear high-density. The melt rheology at 195 °C was measured independently in a rotating-plate rheometer, and the shear viscosity is shown in Fig. 2. Under small-amplitude oscillatory shear, the storage modulus, $G'(\omega)$, exceeds the loss modulus, $G''(\omega)$, at $\omega_c = 8, 30, 700,$ and 800 rad/s for $PS_1, PS_2, PE_1,$ and PE_2, respectively. The extruded

blends are 0.01 mass fraction PS_1 in PE_1, PS_1 in PE_2, and PS_2 in PE_1.

We observe a variety of droplet shapes as a function of $\dot{\gamma}$ and the viscosity ratio $\lambda = (\eta_0)_{PS}/(\eta_0)_{PE}$, where η_0 is the low-$\dot{\gamma}$ viscosity. For PS_2/PE_1 ($\lambda = 240$), spherical droplets elongate along $\hat{x}$ into elliptical shapes that develop a cusplike crease in the equatorial plane at high $\dot{\gamma}$. For PS_1/PE_1 ($\lambda = 22$, upper panel of Fig. 3), similarly shaped droplets exhibit a transition in which they become modestly extended along $\hat{z}$ at high $\dot{\gamma}$. For PS_1/PE_2 ($\lambda = 1.8$, lower panel of Fig. 3), droplets are elongated into thin filaments along $\hat{x}$ that exhibit a transition to wormlike shapes extended along $\hat{z}$ at high $\dot{\gamma}$. The possibility that the shapes arise from complicated flows upstream is ruled out because they reappear upon startup of shear faster than such effects would travel into the channel, and we rule out cavitation because the shapes are not observed in PE melts, both pure and doped with dilute dispersions of micron-sized silica beads.

At the highest $\dot{\gamma}$, the Reynolds number (Re) is less than 10^{-3}. In the low-Re theory of Taylor [1–4], the shape of an initially spherical droplet (radius R_0) is given by
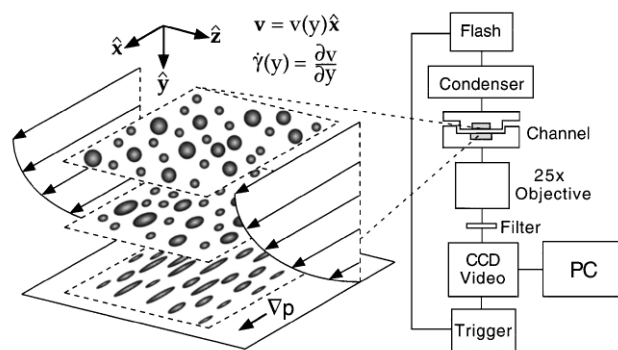

FIG. 1. Geometry of the experiment, where the flow, gradient, and vorticity directions are along $\hat{x}$, $\hat{y}$, and $\hat{z}$, respectively. For a pressure-driven channel flow, the effective shear rate (and thus the local droplet morphology) is a function of y. The CCD camera captures stroboscopic video images in the x-z plane. Coarse and fine micrometer screw adjustment allows the focal plane to be varied as a function of y, and measurements described in this paper are taken at the bottom wall.
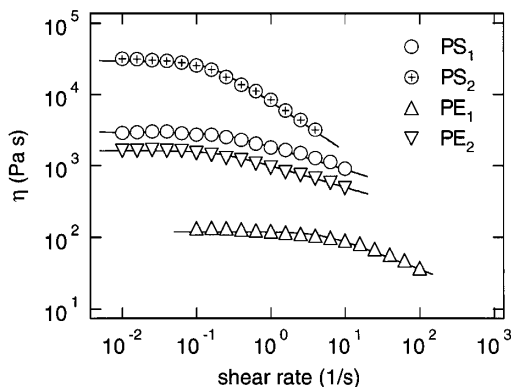
FIG. 2. Steady-shear viscosity as a function of shear rate for the pure melt components at 195 °C, where the fits are as described in the text.

$(L - B)/(L + B) = f_\lambda Ca$, where f_λ is a constant of order unity, and L and B are the longest and shortest droplet dimensions, respectively, in the flow-gradient plane. The capillary number $Ca = \eta R_0 \dot{\gamma}/\kappa$ (where κ is the interfacial tension) measures the strength of the shear stress relative to the capillary pressure [3]. In a phenomenological extension of this approach, we define D to be an ensemble average of $(R_x - R_z)/(R_x + R_z)$, where R_x and R_z are the droplet dimensions along $\hat{x}$ and $\hat{z}$. For droplets elongated along $\hat{x}$, $1 > D > 0$, while for droplets elongated along $\hat{z}$, $-1 < D < 0$. Since larger droplets are more susceptible to the deformation, only those in the largest 5% of the droplet-size distribution are used in the analysis. The data are shown in Fig. 4. The weak-shear fits are to $D = D_0 \tau \dot{\gamma}(D_0 + \tau\dot{\gamma})^{-1}$, which interpolates the low-$\dot{\gamma}$ Taylor regime [14] and the moderate-$\dot{\gamma}$ plateau around D_0. The transition to $D < 0$ corresponds to a coexistence of

the two orientations (upper inset of Fig. 4), suggesting that the intermediate droplet shape becomes metastable in the vicinity of the transition, although this might also be explained by polydispersity in the droplet size.

The diagonal elements of the stress tensor exhibit anisotropy in entangled polymer melts, which can lead to novel effects such as rod climbing [15]. Under simple shear, the low-Re form of the stress tensor for an incompressible viscoelastic fluid is [16]

$$\sigma_{ij} = p\delta_{ij} - \eta\dot{\gamma}\mathbf{e}_{ij} - \psi_1\dot{\gamma}^2\delta_{ix}\delta_{jx}$$
$$- \psi_2\dot{\gamma}^2(\delta_{ij} - \delta_{iz}\delta_{jz}), \qquad (1)$$

where p is the hydrostatic pressure and $\dot{\gamma}\mathbf{e}_{ij} = \partial v_j/\partial x_i + \partial v_i/\partial x_j$. The rheometer measures the normal stress $N = \dot{\gamma}^2(\psi_1 - \psi_2)$, where ψ_1 and ψ_2 are the first and second normal stress coefficients, respectively [16]. Typically, ψ_1 is an order of magnitude larger than ψ_2 [17], and the leading-order behavior is $N \approx \dot{\gamma}^2\psi_1$, with

$$\sigma_{ij} \approx p\delta_{ij} - \eta\dot{\gamma}\mathbf{e}_{ij} - N\delta_{ix}\delta_{jx}. \qquad (2)$$

The normal-stress term thus leads to a stress on the droplet directed along $\hat{x}$ proportional to $-\Delta N = -(N_d - N_c)$, where d and c denote droplet and continuous phase, respectively. For $\Delta N < 0$, the elasticity complements the shear stress, in that it will tend to elongate the droplets along the direction of flow [18]. This might explain why a stringlike morphology is observed at intermediate shear rates for $\lambda = 1.8$, since an emulsion of purely viscous fluids with this viscosity ratio would not be expected to give such an extended droplet shape [1]. If $\Delta N > 0$, N opposes the shear, with $\Delta N(\dot{\gamma}) = 0$ defining a critical shear rate $\dot{\gamma}_c$. For a droplet in compression along $\hat{y}$, the response to a compression along $\hat{x}$ is simply an elongation along the neutral ($\hat{z}$) direction. It can also be argued that
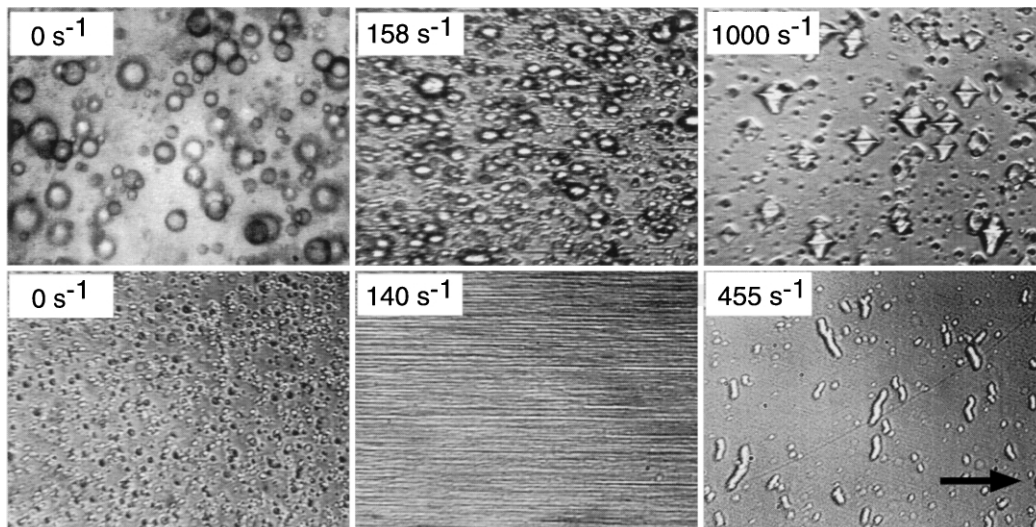

FIG. 3. Droplet morphology as a function of shear rate for 1% PS$_1$ dispersed in PE$_1$ (top) and 1% PS$_1$ dispersed in PE$_2$ (bottom) at 195 °C. The width of each micrograph is 200 μm; $\hat{x}$ is from left to right, $\hat{y}$ is out of the page, and $\hat{z}$ is from top to bottom. For PS$_1$/PE$_2$, the apparent increase in droplet size with increasing shear rate would be explained by shear thinning in the matrix upstream of the channel, where the two components are emulsified.
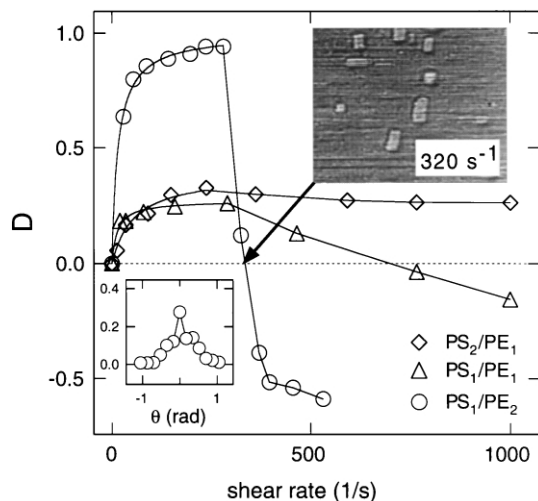
FIG. 4. Average deformation number in the x-z plane vs shear rate for three different PS/PE mixtures at 195 °C, where the fits are as described in the text. Negative D indicates droplets extended, on average, along the vorticity axis. The upper inset shows the morphology of PS_1/PE_2 at the shear rate where D changes sign, where $\hat{\mathbf{x}}$ is from left to right, and the width of the micrograph is 100 μm. The lower inset shows the normalized distribution of droplet orientations for PS_1/PE_2 at 455 s^{-1}, where θ is the measured angle between $\hat{\mathbf{z}}$ and the projection of the mean droplet director onto the x-z plane.
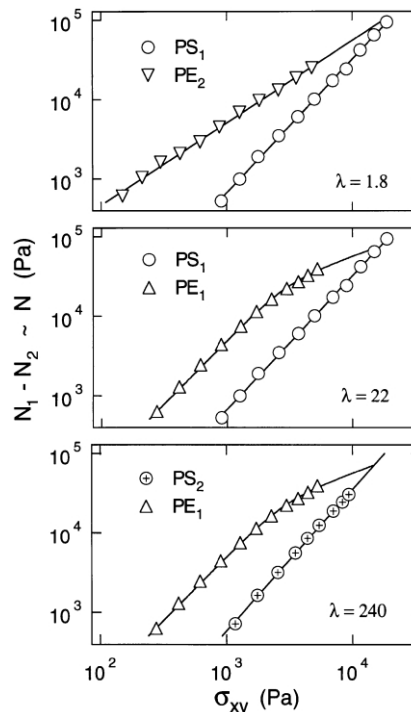

FIG. 5. Normal stress vs shear stress in the pure melt components at 195 °C for each of the blend pairs, where the fits are used to extrapolate the critical shear stress.

vorticity elongation closely resembles the phenomenon of rod climbing. Because of the nonzero shear stress inside a droplet, the internal streamlines will be in tension (the so-called "hoop stress" [16]), which will compress the droplet radially in the flow-gradient plane, causing it to elongate along $\hat{\mathbf{z}}$. If we take $\dot{\gamma}_c$ as the shear rate at which D starts to decrease (Fig. 4), then $\dot{\gamma}_c \approx 280$, 290, and 240 s^{-1} for $\lambda = 1.8$, 22, and 240, respectively. Extrapolating the continuous-phase viscosity to $\dot{\gamma}_c$ using the fits shown in Fig. 2 [19], we obtain $Ca_c \approx 53$, 13, and 11 for $\lambda = 1.8$, 22, and 240, respectively.

Invoking the continuity of tangential stress across the droplet interface, N is plotted as a function of the shear stress (σ_{xy}) in Fig. 5 for each of the pure melt components in each of the three blend pairs. A comparison of N then gives ΔN exactly for a lamellar morphology and provides a leading-order measure for ellipsoidal droplets. Extrapolation to higher σ_{xy} yields $\Delta N \approx 0$ at 25, 17, and 15 kPa for $\lambda = 1.8$, 22, and 240, respectively, in order-of-magnitude agreement with the shear rates obtained above [19]. It is interesting to note that the tendency for vorticity elongation becomes more pronounced with decreasing λ, as evidenced by an increase in the magnitude of the susceptibility $\delta D/\delta \dot{\gamma}$ for $\dot{\gamma} \geq \dot{\gamma}_c$. From the first three data points above the transition ($\dot{\gamma} \geq \dot{\gamma}_c$, Fig. 4) we obtain a slope of -1.5×10^{-2}, -6.1×10^{-4}, and -1.5×10^{-4} s for $\lambda = 1.8$, 22, and 240, respectively. For $\lambda < 1$ (PE in PS) a stringlike pattern [20,21] emerges at low $\dot{\gamma}$ that persists in the limit of strong shear.

Novel and subtle effects associated with droplet deformation in viscoelastic fluids can be found in the literature [22–25]. The results presented here show that such effects can become quite pronounced at high $\dot{\gamma}$. We suggest that vorticity elongation, which bears some resemblance to a phase transition at $\dot{\gamma}_c$, is intimately linked to the viscoelasticity of the melt components. While droplet breakup along the vorticity axis has been suggested for viscoelastic emulsions [22], the stability of such droplets remains unexplored. For dilute suspensions of rigid rods or ellipsoids under shear, a precession of the director around $\hat{\mathbf{z}}$ is observed [26], which would lead to a distribution of director orientations that is peaked around $\pm \theta_{max}$, in contrast to the behavior reported here (lower inset, Fig. 4). A stability analysis as a function of κ and λ would be quite useful.

[1] G. I. Taylor, Proc. R. Soc. London A **138**, 41 (1932); **146**, 501 (1934).

[2] B. J. Bentley and L. G. Leal, J. Fluid Mech. **167**, 241 (1986).

[3] J. M. Rallison, Annu. Rev. Fluid Mech. **16**, 45 (1984).

[4] S. Torza, R. G. Cox, and S. G. Mason, J. Colloid Interface Sci. **38**, 395 (1972); F. D. Rumscheidt and S. G. Mason, J. Colloid Sci. **16**, 238 (1961).

[5] A. Onuki, Phys. Rev. Lett. **62**, 2472 (1989); E. Helfand and G. Fredrickson, Phys. Rev. Lett. **62**, 2468 (1989); S. T. Milner, Phys. Rev. Lett. **66**, 1477 (1991).

[6] X. Wu, D. Pine, and P. Dixon, Phys. Rev. Lett. **66**, 2408 (1991).

[7] E. Moses, T. Kume, and T. Hashimoto, Phys. Rev. Lett. **72**, 2037 (1994).

[8] S. Kim, E. Hobbie, J. Yu, and C. Han, Macromolecules **30**, 8245 (1997).

[9] I. Kadoma and J. van Egmond, Phys. Rev. Lett. **76**, 4432 (1996).

[10] F. Pignon, A. Magnin, and J. Piau, Phys. Rev. Lett. **79**, 4689 (1997).

[11] S. Li, K. Migler, E. Hobbie, H. Kramer, C. Han, and E. Amis, J. Polym. Sci. Polym. Phys. Ed. **35**, 2935 (1997).

[12] The shear rate at the wall can be determined in two ways. Particle-tracking-velocimetry [11] measures the velocity gradient at the bottom window, from which we get $\dot{\gamma}$. Treating the slit die as a capillary rheometer, we compute $\dot{\gamma}$ at the wall from measurements of the volumetric flow rate and pressure drop through the channel. For PE$_2$ melts, the values of $\dot{\gamma}$ determined with these two methods are in reasonable agreement, and here we opt for the latter as it is less labor intensive.

[13] According to ISO 31-8, the term "molecular weight" has been replaced by "relative molar mass" denoted by M_r. The conventional notation rather than the ISO notation has been used in this publication.

[14] From the Taylor theory, $\tau \approx f_\lambda R_0 \eta / \kappa$. Accounting for shear thinning, we obtain $\kappa \approx 9$ mN/m from the weak-shear fits of D for each of the three mixtures, in reasonable agreement with accepted values [see, for example, N. Mekhilef, B. D. Favis, and P. J. Carreau, J. Polym. Sci. Polym. Phys. Ed. **35**, 293 (1997)].

[15] F. H. Garner and A. H. Nissan, Nature (London) **158**, 634 (1946).

[16] See, for example, R. B. Bird, R. C. Armstrong, and O. Hassager, *Dynamics of Polymeric Liquids* (Wiley, New York, 1987), Vol. 1.

[17] M. Doi and S. F. Edwards, *The Theory of Polymer Dynamics* (Oxford University Press, Oxford, 1986).

[18] F. Mighri, P. J. Carreau, and A. Ajji, J. Rheol. **42**, 1477 (1998).

[19] The fit in Fig. 2 is $\eta / \eta_0 = [1 + (\tau_d \dot{\gamma})^2]^{-\beta}$, with $\tau_d = 4.5$, 6.7, 0.2, and 5 s and $\beta = 0.16$, 0.35, 0.2, and 0.15, for PS$_1$, PS$_2$, PE$_1$, and PE$_2$, respectively. For PS$_1$, PS$_2$, and PE$_2$, N (Fig. 5) is fit to $N \sim \sigma_{xy}^\gamma$, with $\gamma = 1.68$, 1.78, and 1.04, respectively. For PE$_1$, the fit is $N \sim \sigma_{xy}^{1.6}[1 + (\sigma_{xy}/\sigma_0)^{3.33}]^{-0.3}$, with $\sigma_0 = 2.88$ kPa. These empirical expressions are used to extrapolate the critical shear stress at which $\Delta N = 0$.

[20] T. Hashimoto, K. Matzusaka, E. Moses, and A. Onuki, Phys. Rev. Lett. **74**, 126 (1995).

[21] A. Frischnecht, Phys. Rev. E **58**, 3495 (1998).

[22] E. Bartram, H. L. Goldsmith, and S. G. Mason, Rheol. Acta **14**, 776 (1975).

[23] H. J. Van Oene, J. Colloid Interface Sci. **40**, 448 (1972).

[24] J. J. Elmendorp and R. J. Maalcke, Polym. Eng. Sci. **25**, 1041 (1985).

[25] L. Levitt, C. W. Macosko, and S. D. Pearson, Polym. Eng. Sci. **36**, 1647 (1996).

[26] G. B. Jeffery, Proc. R. Soc. London A **102**, 161 (1922); B. J. Trevelyn and S. G. Mason, J. Colloid Sci. **6**, 354 (1951).